ELSEVIER

Journal of Nuclear Materials 295 (2001) 281–289

journal of nuclear materials

www.elsevier.nl/locate/jnucmat

Temperature programmed decomposition of thorium oxalate hexahydrate

S. Dash, R. Krishnan, M. Kamruddin, A.K. Tyagi, Baldev Raj *

Metallurgy and Materials Group, Department of Atomic Energy, Indira Gandhi Centre for Atomic Research, Kalpakkam 603 102, TN, India

Received 8 September 2000; accepted 9 January 2001

Abstract

Temperature programmed decomposition (TPD) of thorium oxalate hexahydrate (TOH) was studied by evolved gas analysis-mass spectrometry (EGA-MS), thermogravimetric analysis (TGA) and powder X-ray diffraction (XRD). The microcrystalline solid exhibited sequential dehydration. The anhydrous compound yielded amorphous phase $Th(CO_3)_2$ upon CO release arising out of the bond cleavage. The $Th(CO_3)_2$ phase transformed to nano-crystalline thoria upon decomposition through an oxycarbonate intermediate. The mechanism underlying various conversion stages exhibited control by random nucleation, diffusion and phase boundary interface motion. From the fractional extent of decomposition data, Arrhenius factors like activation energy and pre-exponential factors were evaluated. Based on these studies, a chemical pathway is proposed for the entire decomposition process.

PACS: 28.41.Bm; 81.05.Ys; 81.70.Pg; 82.30.Lp; 82.80.Ms

1. Introduction

Thorium-based fuel cycle involved in advanced heavy-water reactors (AHWR) [1] and fast breeder reactors (FBR) envisages the use of high-density pellets of ThO_2–UO_2 and ThO_2–PuO_2 fuel materials and ThO_2 blanket [2]. A survey shows that oxalate precipitation from the nitrate salt solutions along with the high temperature calcinations is the preferred synthetic route for obtaining high-density nuclear grade-pellets [3]. This route also enables co-processing of mixed oxide (MOX) fuel [4,5]. Metal oxalate hydrates have been extensively used for production of high specific surface metals and metal oxides [6]. With regard to the fuel cycle, two distinct advantages have been cited i.e., improved sinterability of powders and reduced quantities of boron equivalent impurities [7]. In this context, study of the thermal decomposition behavior of the thorium oxalate hexahydrate (TOH) assumes significance. Though metal oxalates have been investigated by many workers [8–10], studies on TOH are rather sparse. There is no report on phase characterization of the various reaction intermediates encountered during decomposition. Also, the kinetics involved in the various conversion sequences have not been determined. Our temperature programmed decomposition (TPD) studies, using evolved gas analysis–mass spectrometry (EGA-MS), thermogravimetric analysis (TGA) and X-ray diffraction (XRD), aim at establishing a comprehensive picture on structural and stoichiometric evolution of thoria from its oxalate precursor. This includes the single particle kinetics as well as the mechanistic aspects of conversion of microcrystalline TOH to nano-crystalline thoria via amorphous intermediate product thorium carbonate.

2. Experimental

TOH manufactured by M/s Reachim and exported by Sojuzchimexport of erstwhile USSR was used in our investigations. The material was finely ground. An ex-

* Corresponding author. Tel.: +91-4114 40 234/40 301; fax: +91-4114 40 301/40 360.

E-mail address: dmg@igcar.ernet.in (B. Raj).

0022-3115/01/$ - see front matter
PII: S0022-3115(01)00481-0

amination by polarized light optical microscopy revealed a particle size distribution centered around 15 μm [11,12]. The trace metallic constituents in this compound were determined using an ELAN 250 inductively coupled plasma-mass spectrometer (ICP-MS) [13]. The samples were dissolved in spectroscopically pure reagents and sprayed to ICP by using a peristaltic pump and Meinhard nebulizer [14]. The data were acquired by rapid scan mode. This instrument was calibrated using synthetic, spectroscopically pure NBS traceable standards. The concentration of the metallic impurities was found to be in the micro-g/g level. The results are presented in Table 1. The preliminary XRD runs indicated powders of TOH to be microcrystalline. The pattern matched with JCPDS-ICDD reported data corresponding to the card number 22-1485.

The EGA-MS experiments on this powdered specimen were conducted in a home-built apparatus. The construction details of this instrument have been published elsewhere [15–17]. However, for the sake of completeness, only a brief description will be furnished here. The facility essentially consists of a high-temperature (~1400 K) – high-vacuum (10^{-6} mbar) programmable resistance furnace coupled to an ultra-high vacuum (UHV) (10^{-10} mbar) chamber through a variable conductance molecular leak valve. A turbomolecular pump is used to evacuate the high-vacuum furnace. The UHV chamber is pumped by an ion-sublimation pump. A separate turbomolecular pump is used for roughing this chamber. The UHV chamber houses quadruple mass spectrometer (QMS), inverted magnetron gauge (IMG) and a spinning rotor viscosity gauge (SRG). The SRG is used for the absolute pressure measurement required for the calibration of QMS and IMG. In high-vacuum furnace, around 100 mg of finely powdered specimen is spread in the form of a thin layer in an alumina crucible. After attainment of the necessary vacuum, the temperature program was issued to heat the specimen, typically at a rate of 5 K/min. The gases evolving from the thermally ramped specimen were detected online by the QMS. An in-house developed software enables dynamic recording of the trend analysis mass spectra as a function of the rising specimen temperature. The TPD spectra of the specimen are obtained by plotting the multiple ion detection mass spectral (MID–MS) signals against the specimen temperature. From these TPD curves, the fractional extent of reaction plots (α–T) was obtained through standard computational procedures [18]. Also, mathematical deconvolution procedures were adopted to resolve the overlapping gas release profiles. The standard commercial softwares like ORIGIN and Peakfit were employed for the deconvolution. The EGA-MS plots were fitted to Gaussian peaks which can be given by the expression

$$Y = a_0 \exp\left[-\left\{ 0.5\left(\frac{x - a_1}{a_2} \right)^2 \right\} \right] \tag{1}$$

and the TGA weight loss steps were fitted to reverse the sigmodal expression given by

$$Y = a_0 \left[1 - \frac{1}{1 + \exp\left\{ 1 - \left(\frac{x - a_1}{a_2} \right) \right\}} \right], \tag{2}$$

where a_0 is the amplitude, a_1 is the center and a_2 is the width of the peak.

In the present TGA investigations, a 0.1 μg sensitivity M/s Setaram, France make Setsys 16/18 thermal analyzer was used. The ultra-high pure helium carrier gas having a flow rate of 40 ml/min provided the sample environment. The TGA runs were carried out at 5 K/min and the sample size was typically 20 mg. Prior to the acquisition of thermograms, the TGA/DTA machine was temperature calibrated by recording the endothermal melting transition of ultra high pure metals like Sn, Zn and Al [19]. The thermograms were corrected for buoyancy and background [20].

For the sake of comparison, the TGA weight loss profile was superimposed on the TPD plots obtained from the EGA-MS. The complex multi-step TGA weight loss profile was mathematically deconvoluted to yield distinct sub-stages. These sub-stages were explained in terms of various gaseous species release data obtained from the EGA-MS spectra. The minor discrepancies between the EGA-MS and the TGA temperatures were observed due to different specimen environments [21]. The kinetic analysis for various stages of conversion was carried out through the use of fractional extent of decomposition parameter α. Except for the early dehydration stage, where α was obtained from the TGA plot, in all other cases α was obtained from the EGA-MS plots. The non-isothermal kinetic methods were used to find out the reaction mechanism

Table 1
Trace metallic impurities in thorium oxalate studied by ICP–MS

Sl. No	Trace element	Concentration in μ-g/g
1	Al	<15
2	Ba	<15
3	Co	<15
4	Cu	<15
5	Cr	<15
6	Fe	<200
7	Mn	<15
8	Mo	<15
9	Ni	<15
10	Pb	<15
11	Sr	<15
12	Ti	<15
13	V	<15
14	Zn	<15

(i.e., the $f(\alpha)$ expressions), activation energy E and the pre-exponential factor Z. This was done by obtaining the best possible correlation with the experimental values obtained from the α–T plots through $\ln\{g(\alpha)/T^2\}$ vs. $1/T$ plots. The analytical expressions for functional transform $f(\alpha)$ and their integral model function $g(\alpha)$ are given in Table 2 [22].

For the purpose of condensed phase characterization of residues by offline XRD, the temperature program was interrupted after various decomposition stages marked by declining of gas release signals to the background on the computer screen. Multiple runs were conducted to collect residues belonging to various stages. These residues were labeled as

Stage A: 300 K – Raw sample of TOH.
Stage B: 340 K – Sample after primary dehydration.
Stage C: 400 K – Sample after secondary dehydration.
Stage D: 600 K – Sample after tertiary dehydration, initial CO release and CO_2 (I) burst.
Stage E: 700 K – Sample after completion of CO release.
Stage F: 750 K – Sample after CO_2 (II) release.
Stage G: 900 K – Sample after completion of CO_2 (III) release.

All the XRD studies were conducted using a Siemens D-500 powder diffractometer. The XRD patterns of powdered samples were obtained using a procedure developed by Rao et al. [23] by spreading the powder specimen on a Si(9 1 1) zero background substrate. The figure of merit of this instrument was checked by acquiring a diffractogram of α-quartz. This is a candidate material, as all its angles are known with considerable accuracy. The line profile broadening analysis of diffraction patterns, after proper correction for instrument broadening, was carried out to establish particle size of the nano-crystalline phase. The mathematical formalism advanced by Scherrer was used for this purpose [24]. This runs as

$$t = \frac{0.9\lambda}{\beta \cos\theta_B}, \tag{3}$$

where t indicates the particle size in nanometer (nm) units and λ refers to the incident X-ray wavelength in nm. In this case, λ was taken to be 0.1541831 nm, which is the weighted average of $Cu(K_{\alpha 1})$ and $Cu(K_{\alpha 2})$ lines. β is the radian measure of the FWHM of the peak at the angle $2\theta_B$ where $2\theta_B$ is the Bragg angle subtended at the maximum intensity.

3. Results and discussion

3.1. EGA-MS and TGA studies

Fig. 1(a) shows the EGA-MS spectra of the compound superimposed with the TGA spectra. Fig. 1(b) shows corresponding fraction release ($\alpha_{(T)} \sim T$) plots obtained from EGA-MS data. These plots indicate fractional extent of condensed phase transformation in terms of release of specific gaseous species water vapor, CO and CO_2, respectively. These plots show on-set and reaction completion temperatures of various decomposition stages. This also clearly indicates that the decomposition by release of CO_2 extends beyond the CO release stage. The EGA-MS spectra of the TOH depict evolution of three distinct profiles. The profile corresponding to the water release ($m/e = 18$) occurs due to

Table 2
Non-isothermal, integral forms of kinetic expression for solid-state reactions

Reaction mechanism	Symbol	$f(\alpha)$	$g(\alpha) = \int_0^\infty d\alpha/f(\alpha)$
Nucleation and growth models			
Random nucleation approach			
(i) Mampel unimolecular law	A1	$1-\alpha$	$-\ln(1-\alpha)$
(ii) Avrami–Erofeev nuclei growth	A(n)	$n(1-\alpha)[-\ln(1-\alpha)]^{1-1/n}$	$[-\ln(1-\alpha)]^{1/n}$
(iii) Branching Nuclei (Prout–Tompkins)	B1	$\alpha(1-\alpha)$	$\ln[\alpha/(1-\alpha)]$
Decelerating Rate Equations			
(a) Based on diffusion mechanism			
(i) one-dimensional diffusion	D1	α^{-1}	$\alpha^2/2$
(ii) two-dimensional diffusion	D2	$[-\ln(1-\alpha)]^{-1}$	$(1-\alpha)[\ln(1-\alpha)]+\alpha$
(iii) three-dimensional diffusion (Jander)	D3	$(1-\alpha)^{-1/3}[1-(1-\alpha)^{-1/3}]^{-1}$	$3/2[1-(1-\alpha)^{1/3}]^2$
(iv) three-dimensional diffusion (Ginstling–Brounshtein)	D4	$[(1+\alpha)^{1/3}-1]^{-1}$	$3/2[1-2\alpha/3-(1-\alpha)^{2/3}]$
(b) Based on Phase Boundary movement			
(i) one-dimensional (Zero-order)	R1	Constant	α
(ii) two-dimensional (cylindrical symmetry)	R2	$(1-\alpha)^{1/2}$	$2[1-(1-\alpha)^{1/2}]$
(iii) three-dimensional (spherical symmetry)	R3	$(1-\alpha)^{2/3}$	$3[1-(1-\alpha)^{1/3}]$

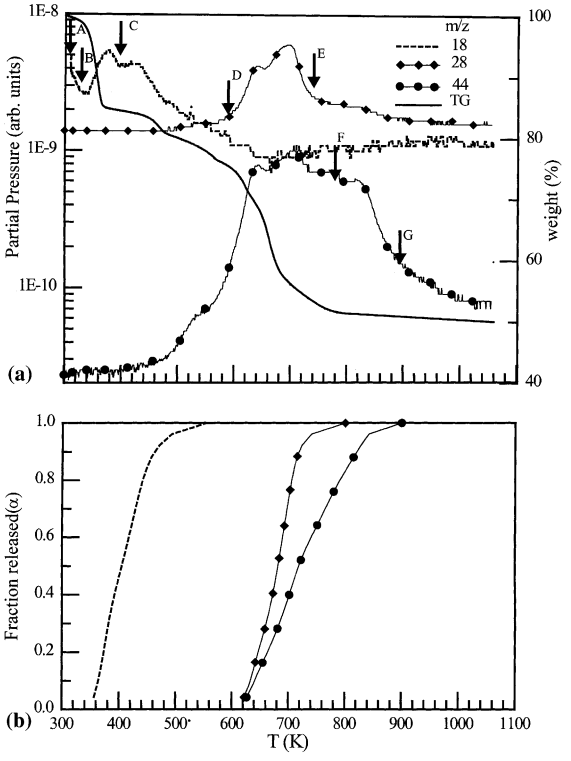

Fig. 1. (a) EGA-MS spectra of the compound superimposed with the TGA spectra. (b) Fraction release plots obtained from the EGA-MS spectra.

dehydration. The profile corresponding to $m/e = 28$ occurs owing to CO release. The $m/e = 44$ profile belongs to CO_2 release. An examination of the oxalate compound removed immediately after vacuum exposure indicated its conversion from the hexahydrate to a dihydrate. In air the dihydrate picks up moisture and gets converted to the hexahydrate again. These dehydration–rehydration phenomena can be ascribed to the loss of four molecules of highly labile lattice librational water. In a similar study, the compound $UO_2(NO_3)_2 \cdot 6H_2O$ has also exhibited this phenomenon [25]. From above observations, it can be stated that the starting material in the vacuum chamber of the EGA-MS furnace was thorium oxalate dihydrate (TOD) where as in TGA experiments the starting material was TOH. In TGA, release of these librational water molecules occurs in the temperature span 320–368 K. This is seen from the deconvoluted TGA spectrum of Fig. 2. A weight loss of 13.3% (stage AB) is explained on the basis of the liberation of four molecules of water. The kinetics, evaluated from the TGA data, indicated control by the random nucleation (A1) mechanism. The activation energy and pre-exponential factors are listed in the Table 3.

A bimodal dehydration profile spanning 340–580 K is seen in the EGA-MS spectra. The deconvoluted de-

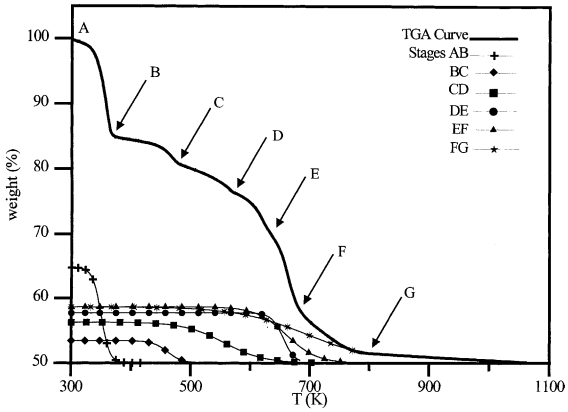

Fig. 2. Deconvoluted TGA spectra depicting various substages.

hydration profile, Fig. 3(a), reveals two stages. The later dehydration stage is somewhat smeared out and partially overlaps with the CO release stage. The dehydration peak I spans 340–500 K with an inflexion at 426 K. The corresponding TGA curve (BC) spanning 368–473K with an inflexion at 462 K amounts to 3.6% weight loss. This can be explained by the release of one molecule of water. The compound converts from dihydrate to monohydrate. This is in agreement with the results reported by Padmanabhan et al. [26]. The mechanism controlling this dehydration step is found to be random nucleation (A1). The Arrhenius parameters evaluated from the fraction release plot are listed in Table 3.

The last dehydration stage indicates conversion of the compound to anhydrous thorium oxalate. The deconvoluted EGA-MS spectra of Fig. 3(a) span 415–580 K with an inflexion at 496 K. The mechanism in this water release stage was found to be two-dimensional phase boundary control (R2). The Arrhenius parameters were determined and listed in Table 3.

The TGA spectra (CD) in the span 473–567 K with inflexion at 554 K depict a weight loss of 6.14%. Also from the EGA-MS spectra, it is seen that there is overlapping release of CO. A burst of CO_2 gas is also seen. This clearly signals the onset of decomposition accruing from the intra-ligand bond cleavage. The 6.14% weight loss is explainable by release of one molecule of water, 1/2 molecule of CO and a burst of CO_2. At this stage, as seen from stoichiometric balance, a substoichiometric anhydrous $Th(C_2O_4)_{2-x}$ compound is formed. From the EGA-MS spectra it is clear that there is a two-stage CO release. The deconvoluted CO release (Fig. 3(b)) shows two peaks. The peak I spans 580–680 K with an inflexion at 632 K. The peak II spans 620–765 K with an inflexion at 695 K. The area ratios turn out to be 1:3. This signifies, that there is a release of two molecules of CO, 1/2 molecule in the stage CD and $1\frac{1}{2}$ molecule in the stage DE. The weight loss profile DE (Fig. 2) amounting

Table 3
Reaction mechanism, correlation coefficient, pre-exponential factor and activation energy

Sl. No	Conversion		Mechanism	Correlation coefficient	Pre-exponential factor (s^{-1})	Activation energy (kJ/mol)
	From	To				
1	TOH	TOD	A1	0.9908	1.4×10^{14}	99.379[a]
2	TOD	TOM	A1	0.99899	2.14×10^{3}	38.564
3	TOM	TOA	R2	0.99993	8.9	21.048
4	TOA	$Th(CO_3)_2$	A1	0.99949	1.53×10^{8}	120.13
5	$Th(CO_3)_2$	$ThOCO_3$	A1	0.99979	2.23×10^{4}	63.802
6	$ThOCO_3$	ThO_2	D3	0.99967	1.14×10^{3}	73.075

[a] TGA value.

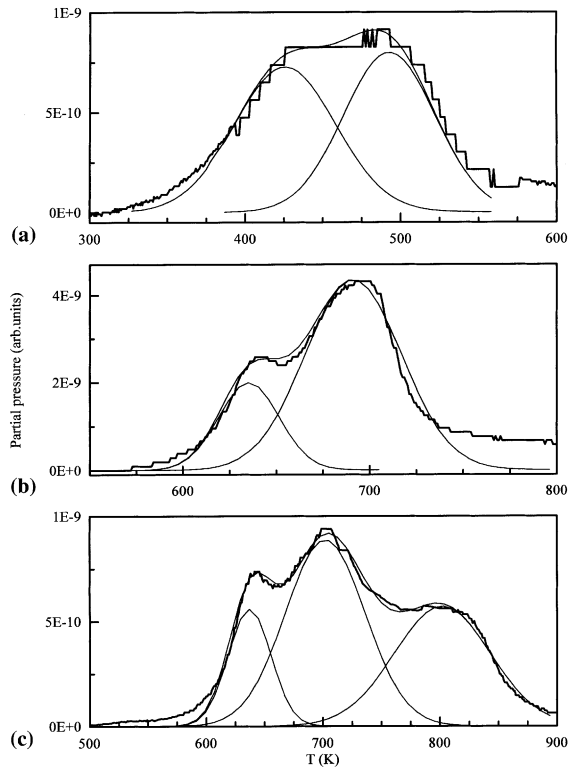

Fig. 3. The deconvolution of the EGA-MS spectra, (a) the dehydration profile, (b) CO release profile and (c) CO_2 release profile.

to 7.7% can be explained on the basis of $1\frac{1}{2}$ molecule of CO release. Once again, the mechanism of release was found to be random nucleation (A1) controlled. The stoichiometric balance indicates conversion of the compound to $Th(CO_3)_2$.

The EGA-MS spectra for CO_2 release span 550–900 K. The spectral deconvolution (Fig. 3(c)) yields three Gaussian peaks centered at 637, 702 and 802 K. The initial stage, as indicated earlier, can be considered as a burst release which signals the decomposition. The two nearly equal-sized release peaks depict a two-stage decomposition of $Th(CO_3)_2$ through CO_2 release. The corresponding TGA spectra (EG), amounting to 17% weight loss, are also a convolution of two equal but distinctly different weight loss stages i.e., EF and FG, each amounting to 8.5%. This amounts to sequential loss of two molecules of CO_2. From the stoichiometric balance it is seen that $Th(CO_3)_2$ converts to $ThOCO_3$ at stage F. Such an oxycarbonate compound has also been reported in an isomorphous actinide oxalate like $Pu(C_2O_4)_2 \cdot 6H_2O$ [27]. $ThOCO_3$ converts to ThO_2 at the stage G. The mechanism of conversion of $Th(CO_3)_2$ to $ThOCO_3$ was found to be random nucleation (A1) controlled, whereas $ThOCO_3$ to ThO_2 conversion was three-dimensional Jander–Mech diffusion-controlled (D3).

3.2. XRD studies

The powder diffractograms of the initial compound as well as its temperature programme derived intermediates are shown in Fig. 4. The microcrystalline samples of raw TOH were found to be triclinic from the XRD studies (Fig. 4(a)). This also matched well with the reported JCPDS-ICDD data card no. 22-1485. A formula molecular unit of the compound contains two bidentate oxalate ligands and two cation bonded water molecules. Four other water molecules are hydrogen bonded as lattice water. The thorium atom appears to be hexa coordinated (Fig. 5(a)). The crystalline architecture is sustained on hydrogen bonding as substantiated from the architecture of many other oxalate ligand bearing compounds [28,29].

The release of the four molecules of water results in the formation of TOD. The basic coordination in the dihydrate is similar to the hexahydrate as seen in Fig. 5(b). The diffractogram of this compound (stage B) matched well with the structure reported vide JCPDS-ICDD card 18-1365 (Fig. 4(b)). The TOD has an orthorhombic structure with four formula molecular units per unit cell [30]. The release of one molecule of water converts the compound to monohydrate (compound at stage C). The schematic of the monohydrate is shown in Fig. 5(c). The corresponding diffractogram in Fig. 4(c)

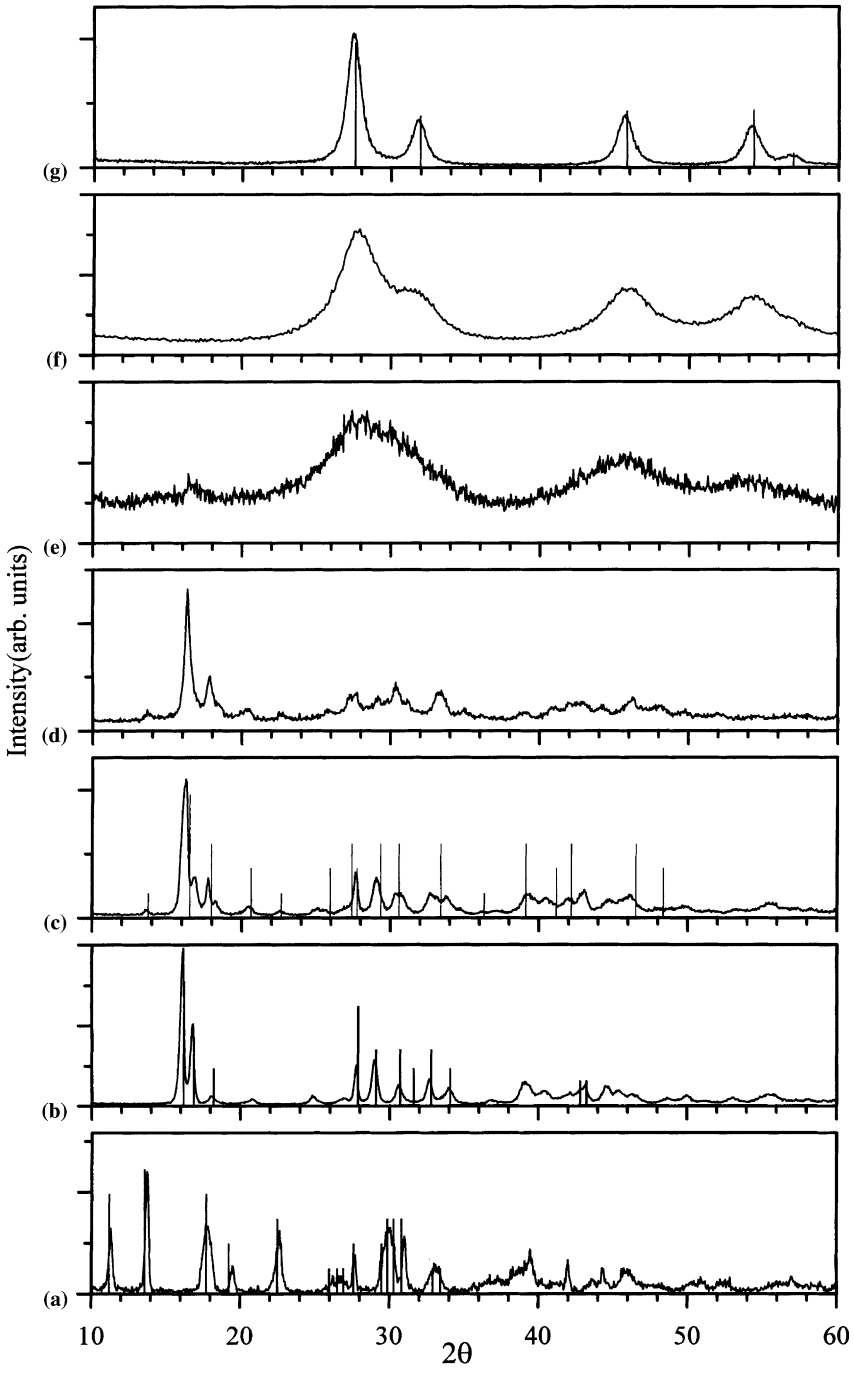

Fig. 4. Powder X-ray diffractograms with corresponding JCPDS-ICDD sticks of (a) TOH, (b) TOD, (c) TOM, (d) TOA, (e) $Th(CO_3)_2$, (f) $ThOCO_3$ and (g) ThO_2.

matched well with the monohydrate data published in the JCPDS-ICDD card 28-1367. The monohydrate also possesses an orthorhombic structure. In comparison to the dihydrate, the monohydrate has a reduced crystal volume. With the advancement of the temperature program to 600 K, the compound, according to the stoichiometric balance, should convert to anhydrous thorium oxalate. The XRD pattern matched well with the pattern reported in the JCPDS-ICDD card 22-1478 (Fig. 4(d)). The structure is orthorhombic with an in-

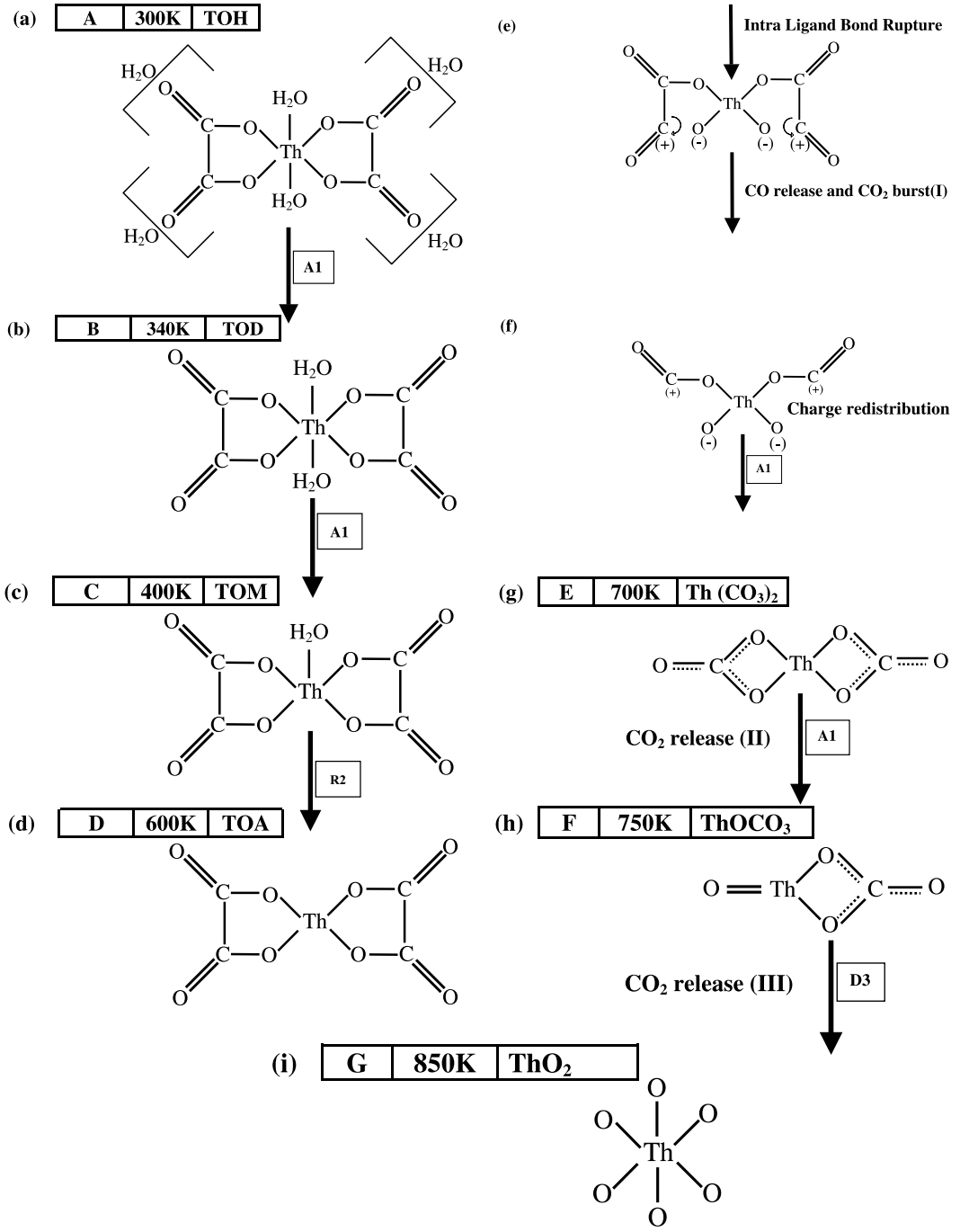

Fig. 5. Crystallo-chemical pathway encountered in the TPD of TOH. A formula molecular unit of (a) TOH, (b) TOD, (c) TOM and (d) TOA. (e) Intra-ligand bond rupture in TOA, (f) Charge redistribution, (g) molecular schematic of $Th(CO_3)_2$, (h) schematic of $ThOCO_3$ and (g) ThO_2 with fluorite structure where Th has an octahedral coordination.

creased crystal volume compared to its predecessor thorium oxalate monohydrate. This implies the formation of more open lattice with renewed coordination around thorium atom. The bond cleavage effects accompanied with the release of CO gas lead to the formation of the stage E residue. The stoichiometric calculations indicate the stage E residue to be $Th(CO_3)_2$. The powder diffraction pattern in Fig. 4(e) depicts an

amorphized product. This diffraction pattern matched with the pattern obtained from the $Th(CO_3)_2$ powders supplied by M/s BDH Chemicals, England. The broad FWHM is an indicator of various conformations of CO_3^- groups present in the different polyhedral units of $Th(CO_3)_2$. A schematic of a formula molecular unit is shown in Fig. 5(g). Many other carbonates like $CaCO_3$ and $BaCO_3$ etc., also depict a certain degree of conformal CO_3^{--} group disorder [31].

The cleavage of the carbonate group occurs in a sequential manner. The advancement of the temperature beyond 750 K results in the formation of the residue F. The stoichiometric balance indicates the formation of $ThOCO_3$ compound. The powder diffraction pattern is shown in Fig. 4(f). The amorphized state of the product is seen in this case also. The persistence of carbonate group disorder is also noticed in this compound. This is inferred from the persistence of broad FWHM. The diffractograms of carbonate and oxycarbonate intermediates are marginally different. Probably, between the two, there is a subtle difference in the coordination around thorium atom.

The completion of decomposition, marked by the diminution of third CO_2 release peak, is noticed around 900 K. The residue exhibited nano-crystalline character. The diffractogram shown in Fig. 4(g) matched well with the JCPDS-ICDD pattern reported for the thoria having a fluorite lattice with octahedrally coordinated thorium atom. The compound has $Fm\bar{3}m$ space group [32]. The average particle size was found to be around 7.5 nm. The crystallo-chemical transformation due to the TPD of the TOH can be addressed in terms of the sequential loss of the water molecules in the dehydration regime. However, the loss of CO molecules consequent to the intra ligand bond cleavage would involve electron transfer and charge redistribution steps [33]. These mechanistic aspects are sketched in Figs. 5(e) and (f). The $Th(CO_3)_2$ and $ThOCO_3$ intermediates, sketched in Figs. 5(g) and (h), probably possess several distorted conformations with distinct topological contrast that prohibits the occurrence of the crystalline order. The transition of the carbonate to oxycarbonate does not change this scenario completely, although marginal difference in the diffractograms indicates a minor change in the coordination around the thorium atom. The formation of large active sites due to amorphization – recrystallization phenomena permit nucleation of the nano-crystalline thoria. Similar trends leading to the formation of ThO_2 nano-crystals have been noticed during the thermal decomposition of $Th(NO_3)_4 \cdot 5H_2O$ [34].

4. Conclusions

The TPD of TOH has been studied by using EGA-MS, TGA and XRD techniques. The gas release data have been used as an indicator of the condensed phase transformation. The TOH indicated a sequential loss of water molecules leading to the formation of anhydrous thorium oxalate. The microcrystalline thorium oxalate anhydrate transformed to amorphous $Th(CO_3)_2$ after the loss of CO from oxalate ligands. The amorphous state persisted in the $ThOCO_3$ residue that after loosing CO_2 got re-crystallized to the nano-crystalline thoria. The non-isothermal kinetics expressions were successfully used to find out reaction mechanism and corresponding Arrhenius parameters for the various stages of conversion.

The calcination procedures adopted for the production of thoria can choose temperature windows from this study to synthesize thoria nano-particles. These non-equilibrium nano-particles depict high inter-granular atomic diffusion rates during the thermal treatments. This vastly enhances the pellet sinterability. Also reduced particle size and high-surface and interfacial energies, associated with the nano-crystals, will ensure better microhomogeniety during the mixed oxide fuel fabrication steps. These aspects may improve irradiation performance of the fuel pellets.

Acknowledgements

The authors are grateful to Dr Placid Rodriguez, Director, Indira Gandhi Centre for Atomic Research for the sustained encouragement. The authors also acknowledge Shri R. Asuvathraman for helping in acquiring X-ray diffractograms and Shri R. Krishna Prabhu for his help in ICP-MS analysis. The authors thank Shri V.S. Sastry for the useful discussions, Shri K. Varatharajan for his assistance in optical microscopy and Shri P.K. Ajikumar for EGA-MS runs.

References

[1] H.P. Vyas, M.L. Dhawan, K. Balakrishnan, D. Saha, K. Anatharaman, in: IAEA-TCM Conference on Advances in Heavy Water Reactors, Mumbai, India, 1990.
[2] S.M. Lee et al., in: India-Japan Seminar on Thorium Utilization, Mumbai, India, 1990.
[3] R.N. Patra, S. Sibasubramanian, in: Proceedings of conference on Power from Thorium: Status, Strategies and Directions (INSAC-2000), vol. 1, Mumbai, India, 2000, p. 6.
[4] K. Sreenivas Rao, P.V. Achuthan, C.V. Narayanan, A. Ramanujam, V.P. Kansra, K. Balu, in: Proceedings of conference on Power from Thorium: Status, Strategies and Directions (INSAC-2000), vol. 1, Mumbai, India, 2000, p. 157.
[5] K. Anantharaman, A. Ramanujam, H.S. Kamath, S. Majumdar, V.N.Vaidya, M. Venkataraman, in: Proceedings of conference on Power from Thorium: Status,

Strategies and Directions (INSAC-2000), vol. 2, Mumbai, India, 2000, p. 107.
[6] D. Dollimore, Thermochim. Acta 177 (1991) 59.
[7] R.E. Lerch, R.E. Norman, Radiochim. Acta 36 (1984) 75.
[8] D. Dollimore, Thermochim. Acta 117 (1987) 331.
[9] N. Kutaish, P. Agarwal, D. Dollimore, Thermochim. Acta 297 (1997) 13.
[10] V. Curles, P. Alphonse, P. Tailhades, A. Rouset, Thermochim. Acta 334 (1999) 107.
[11] H.E. Knechtel, W.F. Kindle, J.L. McCall, R.D. Buchneit, in: T. Lyman (Ed.), Metals Handbook, vol. 8, American Society for Metals, Metals Park, OH, 1973, p. 10.
[12] D.A. Elkington, R. Wilson, in: P.J. Lloyd (Ed.), Particle Size Analysis, Wiley, New York, 1987, p. 261.
[13] T.R. Mahalingam, in: S.K. Aggarwal, H.C. Jain (Ed.), Introduction to Mass Spectrometry, Indian Society for Mass Spectrometry, 1997, p. 13.
[14] S. Vijayalakshmi, R. Krishna Prabhu, T.R. Mahalingam, C.K. Mathews, At. Spectrosc. 13 (2) (1992) 61.
[15] M. Kamruddin, P.K. Ajikumar, S. Dash, B. Purniah, A.K. Tyagi, K. Krishan, Instrum. Sci. Technol. 23 (2) (1995) 123.
[16] M. Kamruddin, P.K. Ajikumar, S. Dash, R. Krishnan, A.K. Tyagi, K. Krishan, Thermochim. Acta 287 (1996) 13.
[17] M. Kamruddin, P.K. Ajikumar, S. Dash, R. Krishnan, A.K. Tyagi, K. Krishan, J. Thermal Anal. 48 (1997) 277.
[18] S. Dash, M. Kamruddin, A.K. Tyagi, Bull. Mater. Sci. 20 (3) (1997) 359.
[19] M. Tisehler, M.J. Koremblit, in: Temperature, its Measurement and Control in Science and Industry, vol. 5, part 1, AIP, New York, 1982, p. 383.
[20] W.W. Wendlandt, in: Thermal Methods of Analysis, Wiley, New York, 1974, p. 29.
[21] P.D. Garn, in: Thermoanalytical Methods of Investigation, Acadamic, New York, 1965, p. 247.
[22] M.E. Brown, in: Introduction to Thermal Analysis, Chapman and Hall, London, 1988, p. 127.
[23] G.V.N. Rao, V.S. Sastry, H.S.G.K. Murthy, V. Seshagiri, T.S. Radhakrishnan, Powder Diffraction 113 (1996) 200.
[24] B.D. Cullity, in: Elements of X-ray Diffraction, Addison-Wesley, Reading, MA, 1956, p. 99.
[25] S. Dash, M. Kamruddin, S. Bera, P.K. Ajikumar, A.K. Tyagi, S.V. Narasimhan, B. Raj, J. Nucl. Mater. 264 (1999) 271.
[26] V.M. Padmanabhan, S.C. Saraiya, A.K. Sundaram, J. Inorg. Nucl. Chem. 12 (1959) 356.
[27] D.A. Nissen, J. Thermal Anal. 18 (1980) 99.
[28] R. Tellgren, J.O. Thomas, I. Olovsson, Acta Crystallogr. B 33 (1977) 3500.
[29] J.O. Thomas, Acta Crystallogr. B 28 (1972) 2037.
[30] I.L. Jenkins, F.H. Moore, M.J. Watermann, J. Inorg. Nucl. Chem. 27 (1965) 81.
[31] H. Chessin, W.C. Hamilton, Acta Crystallogr. 18 (1965) 689.
[32] H. Leigh, E. McCartney, J. Am. Ceram. Soc 57 (1974) 192.
[33] Z. Gabelica, R. Habin, E.G. Derounae, Thermochim. Acta 24 (1978) 315.
[34] S. Dash, M. Kamruddin, S. Bera, P.K. Ajikumar, A.K. Tyagi, S.V. Narasimhan, B. Raj, J. Nucl. Mater. 279 (2000) 173.